

Trimetallic Spinel-Type Cobalt Nickel-Doped Manganese Oxides as Bifunctional Electrocatalysts for Zn-Air Batteries

Soracha Kosasang,^[a, b] Harnchana Gatemala,^[a, b] Nattapol Ma,^[a, b] Praepploy Chomkhuntod,^[a, b] and Montree Sawangphruk^{*[a, b]}

This work demonstrates the effect of trimetallic and bimetallic electrocatalysts of spinel-type metal oxides towards oxygen reduction reaction (ORR) and oxygen evolution reaction (OER). The trimetallic spinel-type $\text{Co}_{0.5}\text{Ni}_{0.5}\text{Mn}_2\text{O}_4$ shows higher bifunctional electrocatalytic activity towards ORR and OER than bimetallic oxides such as CoMn_2O_4 and NiMn_2O_4 . The *in situ* X-ray absorption spectroscopy was applied to observe the change in the oxidation number of Mn, Ni, and Co during the reactions to demonstrate the active metals on the ORR and OER. The Co

plays a more important role in the ORR process than the Ni and Mn, while the three metals exhibit an equivalent contribution on the OER activity as observed from the oxidation state shift. Additionally, the practicality of Zn-air batteries using the trimetallic spinel catalyst is demonstrated to power light-emitting diode and spinning motor with a nominal voltage of 3 V. Bifunctional trimetallic electrocatalysts in this work may be useful for other metal-air batteries.

1. Introduction

Due to a critical concern of climate change, metal-air battery (MAB) is one of the most promising candidates for efficient and clean energy conversion and storage devices that could replace the conventional lithium-ion batteries in electric vehicles (EVs) or even gasoline in combustion engines.^[1] Typically, the theoretical specific energy of Li-ion batteries based on intercalation chemistry is limited at ca. 387 Wh kg⁻¹ ($\text{C}_6\text{Li} + \text{Li}_{0.5}\text{CoO}_2 \leftrightarrow \text{C} + \text{LiCoO}_2$) which is insufficient for long-range EVs.^[2] Whereas, gasoline produced from fossil fuels can generate greenhouse gases leading to global warming problem. The Zn-air battery based on redox reactions has a high theoretical energy density of 1086 Wh kg⁻¹ ($\text{Zn} + \frac{1}{2}\text{O}_2 \leftrightarrow \text{ZnO}$) with additional advantages including low-cost, safety, and environmental friendliness that can attract many attentions.^[2a,b,3] However, practical applications of Zn-air batteries are limited by the slow kinetics of oxygen reduction reaction (ORR) and oxygen evolution reaction (OER) which are the driving reactions of these batteries.^[4] To accelerate these reactions, electrocatalysts with high catalytic activities, high stability, accessibility, and non-toxicity are needed. Although Pt and its alloys are recognized as the superior ORR catalyst and RuO_2 or IrO_2 are reported as the excellent OER

catalyst, their expensive cost and poor cyclability limit their practical utilizations.^[5]

Spinel-type metal oxides are one of the most attractive bifunctional electrocatalysts due to their simple preparation, morphological flexibility and stability. Co_3O_4 with its spinel structure has been developed as highly active electrocatalysts for ORR and OER. Co^{II} in the tetrahedral site is active for the ORR as well as Co^{III} in the octahedral site forms Co–O as active sites for OER.^[6] However, the Co_3O_4 -based catalysts at the air electrodes still suffer from their expensive cost and toxicity.^[7] Manganese oxide-based (MnO_2) catalysts with their structural diversity, low toxicity, and abundance, contain multi-valence states which act as donor-acceptor sites for O_2 adsorption and desorption leading to bifunctional catalytic properties for both ORR and OER.^[8] Typically, the ORR pathway and mechanisms depend on the catalyst and its electronic structure. The direct-four electron and two-electron pathways are influenced by the bidentate and end-on O_2 adsorptions, respectively.^[6] The MnO_2 -based catalysts can promote the two-electron pathway to form peroxide ion intermediate during the ORR which is not favorable for the Zn-air batteries.^[9] On the other hand, Mn^{III}/Mn^{IV} redox couple has been reported as the O_2 acceptor-donor that can occur direct four-electron pathway with a step of proton insertion to form MnOOH and bidentate O_2 adsorption to generate OH⁻.^[9-10] Besides the spinel-type single metal oxides (A_3O_4), the bimetallic ($\text{A}_x\text{B}_{3-x}\text{O}_4$) and trimetallic ($\text{A}_x\text{B}_y\text{C}_{3-x-y}\text{O}_4$) metal oxides have played a role in bifunctional electrocatalytic activities on both ORR and OER.^[6] The replacement or insertion of another metal into the A_3O_4 material is one of the best strategies to tune the structural and electronic properties of the oxide materials which can improve the ORR and OER catalytic performances.

In this work, we demonstrated the influence of spinel-type metal oxide materials which are bimetallic (NiMn_2O_4 and CoMn_2O_4) and trimetallic ($\text{Co}_{0.5}\text{Ni}_{0.5}\text{Mn}_2\text{O}_4$) metal oxides on the

[a] S. Kosasang, H. Gatemala, N. Ma, P. Chomkhuntod,
Prof. Dr. M. Sawangphruk
Department of Chemical and Biomolecular Engineering
School of Energy Science and Engineering
Vidyasirimedhi Institute of Science and Technology
555 Moo 1 Payupnai, Wangchan District, Rayong 21210, Thailand
E-mail: montree.s@vistec.ac.th

[b] S. Kosasang, H. Gatemala, N. Ma, P. Chomkhuntod,
Prof. Dr. M. Sawangphruk
Center of Excellence for Energy Storage Technology (CEST)
Vidyasirimedhi Institute of Science and Technology
555 Moo 1 Payupnai, Wangchan District, Rayong 21210, Thailand

 Supporting information for this article is available on the WWW under
<https://doi.org/10.1002/batt.202000006>

ORR and OER catalytic activities. Additionally, the effect of mixed phases in $\text{Co}_{0.5}\text{Ni}_{0.5}\text{Mn}_2\text{O}_4$ materials produced at different calcined temperature was studied and further identified during the ORR and OER processes by *in situ* X-ray absorption spectroscopy (XAS). Moreover, the performances of Zn-air batteries using $\text{Co}_{0.5}\text{Ni}_{0.5}\text{Mn}_2\text{O}_4$ and the state-of-art Pt/C + RuO₂ were measured by the galvanostatic discharge-charge technique and tested in the real application by powering the 3 V light-emitting diode (3 V LED).

Experimental section

Chemicals and materials

Potassium permanganate (KMnO_4), cobalt nitrate hexahydrate ($\text{Co}(\text{NO}_3)_2 \cdot 6\text{H}_2\text{O}$), sodium hydroxide (NaOH) were purchased from Ajax Finechem. Tannic acid ($\text{C}_{76}\text{H}_{52}\text{O}_{46}$) was obtained from Carlo Erba Reagents while polyvinylidene fluoride (PVDF) and nickel chloride hexahydrate ($\text{NiCl}_2 \cdot 6\text{H}_2\text{O}$) were obtained from Sigma Aldrich. N-methyl-2-pyrrolidone (NMP) was purchased from Merck. All chemicals are analytical grade and used as received. Deionized (DI) water (Milli-Q, 15 MΩ cm) was used as a solvent.

Synthesis of CoNi-doped manganese oxides

CoNi-doped manganese oxides were synthesized using our previous protocol.^[11] Briefly, CoNi-doped MnCO_3 microdumbbells were prepared via the hydrothermal process. A metal solution precursor was prepared by mixing 2.878 g of $\text{Co}(\text{NO}_3)_2 \cdot 6\text{H}_2\text{O}$, 2.3507 g of $\text{NiCl}_2 \cdot 6\text{H}_2\text{O}$ and 6.25 g of KMnO_4 in 200 mL of DI water (mole ratio of $\text{Co:Ni:Mn} = 0.5:0.5:2$). Another solution was 3.125 g of tannic acid for which its pH was adjusted pH to 7 and its volume was adjusted to be 200 mL with DI water, and then gradually added into the metal solution with stirring continuously for 10 min. The resulted mixture was transferred into 500 mL Duran bottle and incubated at 80 °C for 12 h. A precipitate of CoNi-doped MnCO_3 was cleaned with DI water several times and dried at 60 °C for 24 h. Consequently, metal carbonate compound was applied as a template for CoNi-doped manganese oxides preparation via calcination at 500°, 700° and 900°C for 5 h (5 °C min⁻¹) under air atmosphere and dry at room temperature.

Physicochemical characterizations

Morphology (size and shape) of the materials was investigated by a field emission scanning electron microscope (FE-SEM: JEOL, JSM-7001F) performing at 1 kV under a high vacuum mode with a secondary electron image (SEI) detector. Transmission electron microscopy (TEM, Hitachi operated at 120 kV) and energy dispersive X-ray spectrometer (EDS) were applied to observe the morphology and analyze the elemental distribution and composition of all materials. Bruker D8 ADVANCE instrument was utilized to identify the X-ray diffraction (XRD) patterns of samples using Cu K α radiation (40 kV, 40 mA) with a step size of 0.01° in the 2θ range of 5–80°. Wavelength dispersive X-ray fluorescence (WDXRF, S8 Tiger, Bruker) was performed to determine the quantitative elemental ratio of materials. X-ray photoelectron spectroscopy (XPS, Axis Ultra DLD, Kratos Analytical Ltd., with Al-K alpha radiation ($h\nu = 14,866$ eV)) was utilized to study the surface chemistry of the materials.

Electrochemical evaluation

The catalyst slurry was obtained by mixing 20 mg of active catalyst powder and 20 mg of carbon black in 600 μL of 0.6% of PVDF in NMP. The mixture was sonicated for 2 h before dropping and drying on the rotating disk electrode (RDE). The catalyst loading was ca. 0.1 mg cm⁻². The electrocatalytic activities (oxygen reduction reaction (ORR) and oxygen evolution reaction (OER)) were tested via linear sweep voltammetry (LSV) in 0.1 M KOH solution under O₂ and Ar saturation. Note, the electrochemical experiments were measured via computer-controlled μ-AUTOLAB II potentiostat (Eco-Chemie, Utrecht, The Netherlands) equipped with a FRA2 frequency response analyzer module and run on NOVA software (version 1.11). The conventional three-electrode cell was used in this system including a platinum wire as the counter electrode, a saturated calomel electrode (SCE) as the reference electrode, and a catalyst-coated GC as the working electrode. Moreover, the Zn-air batteries were tested via the galvanostatic discharge-charge technique at a current density of 2, 3, 5, and 10 mA cm⁻² with 10 min and 2 h per cycle.

In situ electrochemical X-ray absorption spectroscopy (XAS) measurements

The changes in the oxidation numbers of Mn, Co and Ni were determined using the *in situ* fluorescent mode of the XAS technique performed at beamline No. 5, Synchrotron Light Research Institute (Public Organization), Nakhon Ratchasima, Thailand. The Ge (220) double-crystal monochromator in an energy range of 3440–12,100 eV was used to collect the X-ray energy. The direction of the 4-element silicon drift detector was set at 90° to the beam and 45° to the sample for spectroscopic data collection. The Mn, Co and Ni meshes were applied as standards for the calibration of the K-edge Mn, Co, and Ni at 6539, 7709, 8333 eV, respectively. The light dimension hitting the sample was adjusted to 5 mm in width and 1 mm in height. The working electrode employed for the XAS measurement was prepared by coating a catalyst slurry on carbon fiber paper (CFP) at ~0.3 mg cm⁻². O₂ gas was flowed into 0.1 M KOH solution for 40 min before applying a constant potential via the chronoamperometric method to the working electrode. The measurement was started after observing a constant response current. This measurement can provide a change in the oxidation number of metals during ORR and OER.

2. Results and Discussion

2.1. Physicochemical Properties

Figure 1a, b, and c show SEM images of the trimetallic cobalt nickel-doped manganese oxides (CNM) under calcination at 500 (CNM@500), 700 (CNM@700), and 900°C (CNM@900), respectively. The morphologies are significantly different depending on the calcination temperature. The CNM@500 has a dumbbell-like shape with a very rough surface while the surface of CNM@700 is nearly smooth and finally smooth at the high temperature of 900°C (CNM@900). The structures of the materials were confirmed by XRD patterns (Figure 1d), suggesting that the spinel-type materials and the composition ratios were identified by the WDXRF corresponding to $\text{Co}_{0.5}\text{Ni}_{0.5}\text{Mn}_2\text{O}_4$ (Table S1). The XRD pattern of the CNM@500 consists of three phases which are $\text{Co}_{0.5}\text{Ni}_{0.5}\text{Mn}_2\text{O}_4$, NiMnO_3 , and Mn_2O_3 phases. The peaks at 20~18.3, 30.1, 35.5, 36.1, 37.1, 43.3, 53.7, 57.1,

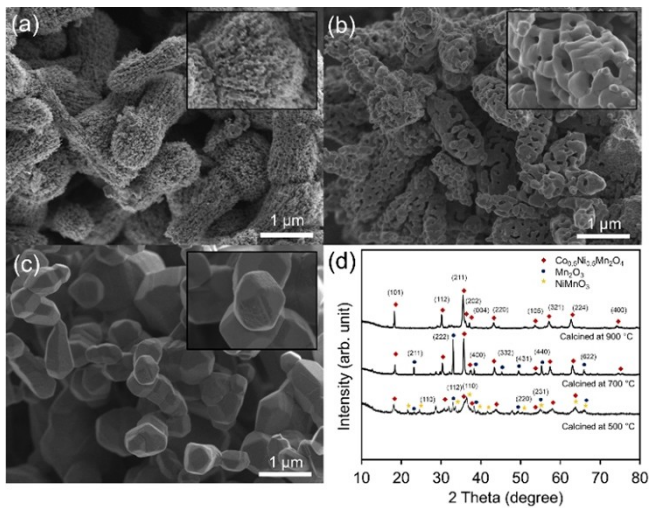


Figure 1. SEM images of a) CNM@500, b) CNM@700, c) CNM@900, and d) XRD patterns of the spinel-type metal oxides.

62.7, and 74.0° are assigned to (101), (112), (211), (202), (004), (220), (105), (321), (224), and (400) planes, respectively, corresponding to the spinel metal oxide.^[12] The appearance of NiMnO_3 and Mn_2O_3 phases can be observed at the defined peaks in Figure 1d.^[13] After increasing the calcined temperature to 700°C (CNM@700), the NiMnO_3 phase was disappeared. The Mn_2O_3 phase was then eliminated by enhancing calcination temperature at 900°C to obtain the pure phase of the spinel $\text{Co}_{0.5}\text{Ni}_{0.5}\text{Mn}_2\text{O}_4$. To further observe the particle shape and lattice planes of the materials, TEM was employed. TEM images are in a good agreement with the SEM images that the CNM@900 shows larger particles as compared to the CNM@700 and CNM@500, respectively (Figure 2). The EDS mapping of the trimetallic materials displays the elemental distribution of the Co, Ni, and Mn (Figure 2b-o), suggesting the well-dispersed elements in all samples. Besides, the SEM images and XRD patterns of pure $\text{CoNi}-\text{MnCO}_3$ template, NiMn_2O_4 (NM@900), and CoMn_2O_4 (CM@900) are shown in Figure S1.^[14] Elemental composition and oxidation state of the CNM materials were further investigated via the XPS as demonstrated in Figure S2. The Mn 2p XPS exhibits two peaks corresponding to two pairs of spin-orbit doublets of Mn 2p_{3/2} (642.3 eV) and Mn 2p_{1/2} (653.7 eV) with the spin-orbit splitting of 11.4 eV.^[15] The Mn 2p_{3/2} XPS spectra can be deconvoluted into three peaks at 640.4, 641.9, and 643.4 eV assigned to Mn²⁺, Mn³⁺, and Mn⁴⁺, respectively. The Co 2p XPS spectra can be fitted into two peaks at 780.3 and 781.3 eV of Co²⁺ and Co³⁺, respectively.^[16] Two satellite (sat) peaks at ~787 and 784 eV represent the presence of Co³⁺ and the existence of the Co²⁺, respectively.^[17] Likewise, the Ni 2p_{3/2} XPS spectra of all materials can be deconvoluted into two peaks of Ni³⁺ (~855.9 eV) and Ni²⁺ (~854.9 eV) along with the Ni satellite peak at 861.7 eV.^[17]

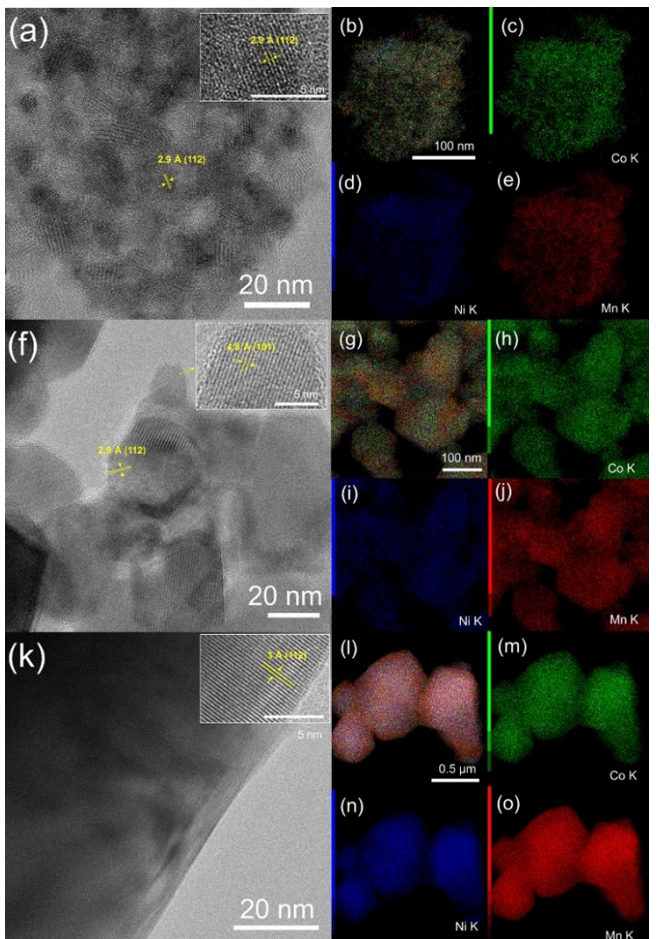


Figure 2. TEM images of a) CNM@500, f) CNM@700, and k) CNM@900 and EDS mapping of Co, Ni, and Mn elemental distribution of b–e) CNM@500, g–j) CNM@700, and l–o) CNM@900.

2.2. Electrochemical Property

The ORR and OER catalytic activities were evaluated via cyclic voltammetry (CV) and linear sweep voltammetry (LSV) under Ar- and O₂-saturated 0.1 M KOH solution. The CV measured under a saturated O₂ condition shows a significant reduction peak, as compared to the CV under a saturated Ar condition, indicating that there is an occurrence of the ORR (Figure S3a). The LSV of ORR catalytic activity is measured at a scan rate of 10 mVs⁻¹ in the potential range of 1 to 0 V vs. RHE, while the potential range of the LSV of OER is from 1.2 to 2 V vs. RHE. The catalytic activities of both ORR and OER can be observed from the onset potential (E_{on}), half-wave potential ($E_{1/2}$) and potential at a current density of 10 mA cm⁻² (E_{10}).^[18] The E_{10} values of the CNM@900, CM@900, and NM@900 are 1.78, 1.79, and 1.89 V vs. RHE, respectively. The more negative potential of the OER indicates the lower overpotential, suggesting the higher OER catalytic performance of the trimetallic material.^[1a,19] Also, the pure trimetallic CNM@900 demonstrates better ORR catalytic activity as compared to the bimetallic samples which can be observed from the more positive E_{on} and $E_{1/2}$ (Figure 3b).^[20] Therefore, the trimetallic catalyst has better bifunctional

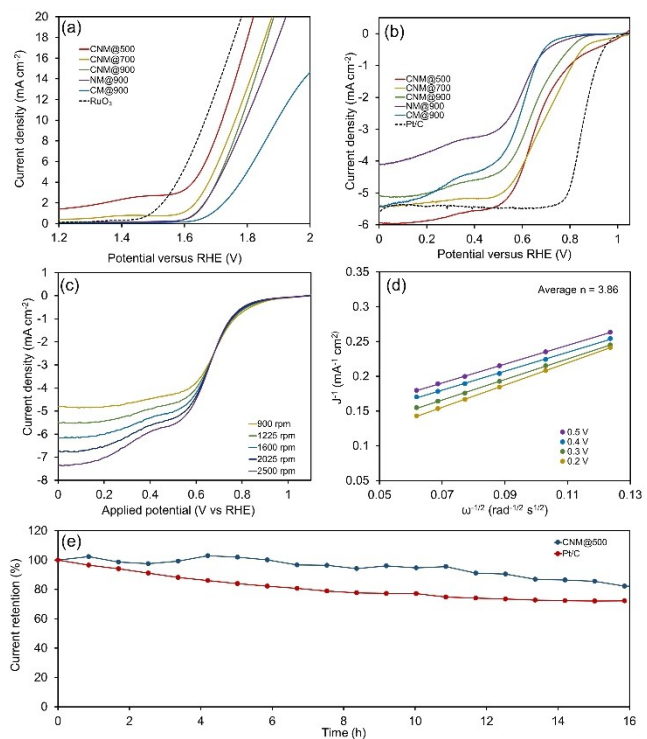


Figure 3. Electrochemical measurements of a) LSV of OER, b) ORR measured at a scan rate of 10 mV s^{-1} and a rotating rate of 1600 rpm in O_2 -saturated 0.1 M KOH solution, c) LSV at various rotation rates, d) K-L plot of CNM@500, and e) current retention of the catalysts at a constant potential of 0.67 V vs. RHE.

catalytic activities than the bimetallic catalysts. Furthermore, the catalytic performances of the trimetallic catalysts at different calcined temperature with various phases were studied. The E_{10} values of CNM@500, CNM@700, and CNM@900, are 1.72, 1.76, and 1.78 V vs. RHE, respectively, suggesting the highest OER catalytic activity of the CNM@500. The $E_{1/2}$ values of CNM@500, CNM@700, CNM@900, NM@900, and CM@900 are 0.65, 0.71, 0.64, 0.61, and 0.60 V vs. RHE, respectively. Moreover, the OER (ORR) kinetics could be suggested from the Tafel plot for which the Tafel slopes of the CNM@500, CNM@700, CNM@900, NM@900, and CM@900 are 220.9 (137.4), 228.7 (135.5), 236.4 (145.3), 236.8 (166.6), and, 243.2 (163.5) mV dec^{-1} , respectively (Figure S3b–c). The lower Tafel slope can suggest a higher catalytic activity.^[21] Besides, the state-of-art Pt/C shows the $E_{1/2}$ and Tafel slope for the ORR of 0.86 V vs. RHE and 71.7 mV dec^{-1} , respectively. The RuO₂ exhibits the E_{10} of 1.67 V vs. RHE along with its Tafel slope of $191.0 \text{ mV dec}^{-1}$. Additionally, the electrochemical double-layer capacitance (C_{dl}) of the materials is calculated as demonstrated in the supporting information section.^[22] The C_{dl} values of the CNM@500, CNM@700, and CNM@900 are 10.9, 5.5, and $3.1 \mu\text{F cm}^{-2}$, respectively, indicating the higher electrochemical surface area of the CNM@500 (Figure S4).^[22–23] Moreover, the number of transfer electron per oxygen molecule (n) is an important parameter to suggest the superior ORR catalyst which can be calculated by the Koutecky-Levich (K-L) equation (See the Supporting information section).^[8,24] Figure 3c shows the LSV at

different rotation speeds of the CNM@500 along with the K-L plot (Figure 3d).

The calculated n is equal to 3.86, suggesting the four-electron pathway of the ORR for the CNM@500. The electrochemical impedance spectroscopy (EIS) was also studied in a frequency range of 100,000 Hz–0.01 Hz with an amplitude of 5 mV to indicate the kinetics and interfacial properties of the catalysts. An equivalent circuit model includes a frequency-dependent constant phase element (CPE) instead of a capacitor due to the surface and porosity inhomogeneity of the atomic level with the heterogeneous charge arrangement on the electrode surface.^[25] The other parameters including electrolyte resistance (R_s), an oxide film resistance (R_f), a charge-transfer resistance (R_{ct}) are also involved in the equivalent circuit.^[26] The Nyquist plots show the simulated curves fitted with the data point. The R_{ct} values of CNM@500, CNM@700, and CNM@900 are 38, 40, and, 77 Ω , respectively, suggesting the higher rate reaction of CNM@500 electrode as compared to the others (Figure S5a).^[27] Additionally, methanol tolerance curves of the CNM@500 and CNM@700 exhibit only ~10% lower catalytic activity, while the catalytic activity of CNM@900 shows 24% decrease in the presence of 0.1 M MeOH as compared to the absence of MeOH in 0.1 M KOH solution (Figure S5b). Moreover, the stability of the catalysts was tested via a chronoamperometry technique at an applied constant potential of 0.67 V vs. RHE. The CNM@500 demonstrates better current retention as compared to the commercial Pt/C. The current retentions of the CNM@500 and the commercial Pt/C are 82.3 and 72.2% after 16 h. Besides, the comparison between the CNM@500 and other previous reported bifunctional catalysts towards the ORR and OER are demonstrated in Table S2 in the supporting information section.^[28]

2.3. In Situ X-ray Absorption Spectroscopy

To further understand the role of the metals in the trimetallic CNM materials, the *in situ* XAS was applied to demonstrate the change in the oxidation states of the Mn, Co, and Ni elements during the ORR and OER processes. The X-ray absorption of Mn K-edges has been extensively applied for studying the structure and valence in various compounds which can provide the average oxidation state of the metal centers.^[29] For example, $\text{CaMn}^{III} \text{O}_4$ with the mean oxidation state observed from XAS is equal to +3.8 indicating that this material contains primarily Mn^{IV} cations with ~20% of Mn^{III} ions.^[30] The catalysis involves the atoms on the surface such as the dioxygen formation is introduced by the oxidative charging of the CaMn_2O_4 catalyst through the oxidation of Mn^{III} to Mn^{IV}.^[30–31] Note, the higher near-edge absorption energy implies the more positive charge in the material.^[32] The change in oxidation states during the ORR and OER as compared to the initial state can suggest the difference between the population number of various valence states which may relate to the metal center participated in the reactions.^[29c,33] Figure 4 shows X-ray absorption near edge structure (XANES) of the Mn, Co, and Ni elements which can observe the shifts in the edge positions to the lower energy

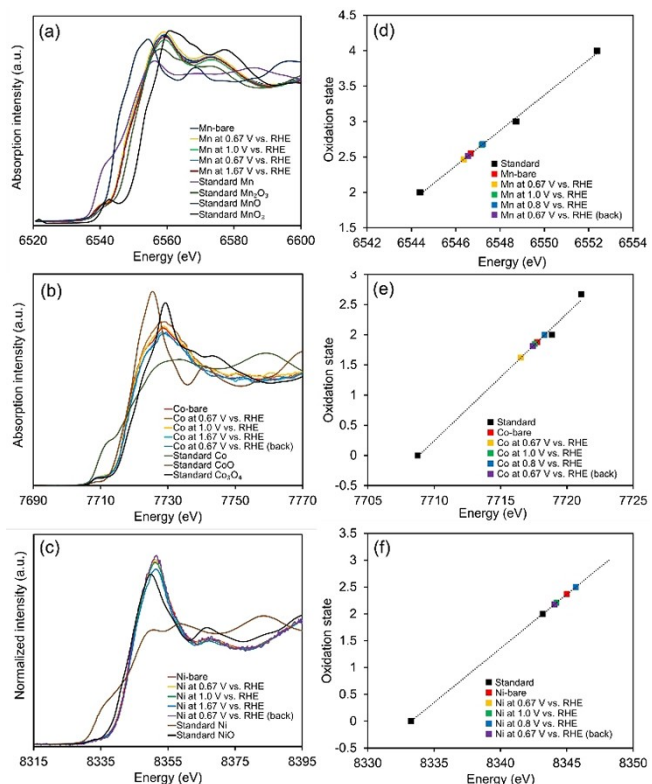


Figure 4. XAS spectra of a) Mn K-edge, b) Co K-edge, and c) Ni K-edge of the CNM at various applied potentials and the oxidation state changes of d) Mn, e) Ni, and f) Co during applying potentials for the ORR and OER.

during the ORR process as compared to the bare Mn, Co, and Ni, suggesting the reduction reactions of the metal ions.^[29c] On the other hand, positive shifts are observed during the OER process, indicating the oxidation reaction occurred in the Mn, Co, and Ni. Figure 4a shows the shifts in the edge positions of the Mn during the ORR and OER compared to the standard $Mn^{(II)}O$, $Mn_2^{(III)}O_3$, and $Mn^{(IV)}O_2$ which can indicate the oxidation states of the bare Mn, the Mn during the ORR, and OER processes. The average oxidation number of the original Mn in the CNM is $Mn^{2.55+}$ which is reduced to $Mn^{2.47+}$ during the ORR (at 0.67 V vs. RHE) and increased to $Mn^{2.68+}$ during the OER (Figure 4d). The reversibility of Mn is proved by the returned $Mn^{2.51+}$ after applying the returned 0.67 V vs. RHE. Likewise, the oxidation states of the bare Co, during the ORR, and OER as compared to the standard are $Co^{1.88+}$, $Co^{1.62+}$, and $Co^{2.00+}$, respectively, as well as the returned Co oxidation state after applying the ORR potential, is $Co^{1.81+}$ (Figure 4e). The average oxidation numbers of the Ni are also identified similar to the Mn and Co. The valence states of the pristine Ni, the Ni during the ORR, and OER are in between the standard NiO and Ni which are equivalent to $Ni^{2.36+}$, $Ni^{2.21+}$, $Ni^{2.50+}$, respectively. The returned Ni oxidation state after applying the ORR potential is $Ni^{2.17+}$ (Figure 4f). Therefore, the oxidation state shifts of the Mn, Co, and Ni during the ORR are 0.08, 0.26, and 0.15, respectively while during the OER they are 0.13, 0.12, and 0.14 as compared to the bare Mn, Co, and Ni, respectively (Figure S6). Hence, the Co plays a more important role on the ORR

process than the Ni and Mn, while the three metals play an equivalent role on the OER process as observed from the difference in an oxidation state change.

2.4. Zn-Air Batteries

To demonstrate the usability of the new materials, Zn-air batteries were fabricated using the CNM@500 and the state-of-art Pt/C + RuO₂ as illustrated as a configuration in Figure 5a. Open circuit potentials (OCP) of Zn-air batteries using the CNM@500 and the Pt/C + RuO₂ are stable over 6 h at 1.36, and 1.40 V vs. Zn/Zn^{2+} , respectively (Figure 5b). The discharge-charge polarization curves of the Zn-air batteries using the CNM@500 and CNM@700 show smaller discharge-charge voltage range as compared to the CNM@900 in which the power densities of these batteries are 49, 45, and 30 $mW\text{cm}^{-2}$, respectively (Figure S7a-b). The specific capacities of the Zn-air batteries using the CNM@500, CNM@700, and CNM@900 measured at a discharge current density of 5.2 mAcm^{-2} and normalized to the consumed mass of Zn (Figure S7c) are 876.4, 848.3, and 808.9 $\text{mAh}_{\text{Zn}}^{-1}$ which are equivalent to energy densities of 972.8, 941.6, and 687.6 $\text{Wh kg}_{\text{Zn}}^{-1}$, respectively. The discharge-charge profiles of the Zn-air batteries were measured at a current density of 2 mAcm^{-2} (2 h per cycle) and displayed in Figure 5c. The potential gap between discharge and charge potentials (ΔE) of the Zn-air battery using CNM@500 is equal to 0.75 V, while the ΔE of the Zn-air battery using the Pt/C + RuO₂ is 0.67 V at the first cycle. Although the Zn-air battery using the

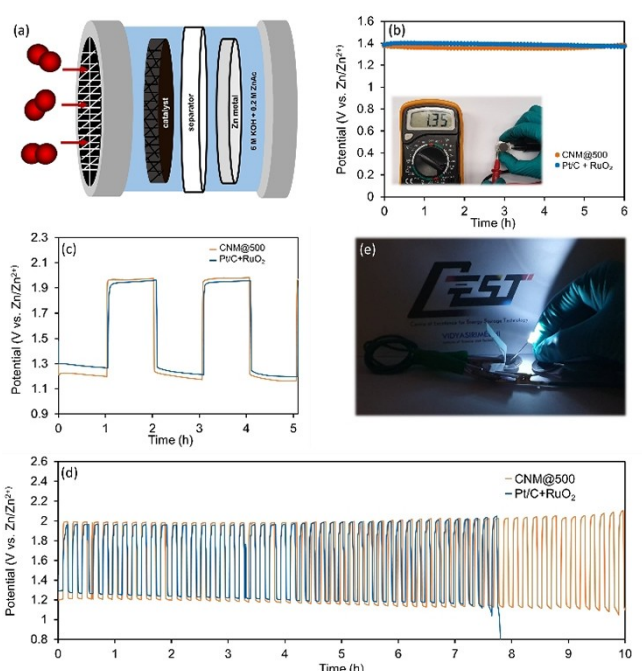


Figure 5. Zn-air batteries: a) cell configuration, b) open circuit potential (OCP), c) discharge-charge profiles at a current density of $2 \text{ mA}\text{cm}^{-2}$ with 2 hours per cycle, d) cyclability of the Zn-air batteries using CNM@500 and Pt/C + RuO₂ at a current density of $2 \text{ mA}\text{cm}^{-2}$ with 10 minutes per cycle, and e) three Zn-air batteries using CNM@500 in a series powering the 3 V LED.

Pt/C + RuO₂ exhibits a higher performance than the Zn-air battery using CNM@500, Zn-air battery using our bifunctional electrocatalyst shows better stability. Zn-air batteries using Pt/C + RuO₂ and CNM@500 have a cyclability of over 8 and 10 h, respectively, as displayed in Figure 5d. Moreover, the stability test of the Zn-air battery using CNM@500 at various current densities of 3, 5, and 10 mA cm⁻² demonstrates the durability of over 12, 8, and 4 h, respectively (Figure S7d-f). For the proof of concept, Zn-air battery using the CNM@500 was applied in the real application of light-emitting diode (LED; 5 mm, ≈3.2 V) with three cells connected in a series as shown in Figure 5e. Furthermore, the comparison between the Zn-air battery using the CNM@500 and other reported Zn-air batteries is demonstrated in Table S3 in the supporting information section.^[5c,28c,29e,34]

3. Conclusions

In summary, the catalytic activities of the trimetallic spinel cobalt nickel-doped manganese oxides (Co0.5Ni0.5Mn₂O₄) are demonstrated as compared to the bimetallic spinel materials (CoMn₂O₄ and NiMn₂O₄). The trimetallic catalysts exhibit better bifunctional catalytic performances towards ORR and OER. The superior catalytic activities of the trimetallic samples are due to the active Co for the OER active site coupled with the Mn and Ni for the ORR active sites as observed from the in situ XAS. The oxidation number changes during the reactions suggest the oxidation and reduction of the Mn, Co, and Ni which are equivalent to 0.08, 0.26, and 0.15 for the ORR as well as 0.13, 0.12, and 0.14 for the OER, respectively. Additionally, the calcined temperature on the CNM synthesis has an influence on the morphology and the electrochemically active surface area, leading to the better catalytic activity of the CNM@500. Moreover, Zn-air batteries using the CNM@500 and state-of-art Pt/C + RuO₂ as the bifunctional catalysts are demonstrated and compared. The Zn-air battery using the CNM@500 shows a better cyclability than the Pt/C + RuO₂. Interestingly, the Zn-air battery using CNM@500 works very well in the real demonstration, which can provide power to 3 V LED (3 cells in a series).

Acknowledgements

This work was financially supported by the Thailand Research Fund and Vidyasirimedhi Institute of Science and Technology (RSA6180031) as well as Energy Policy and Planning Office (EPPO), Ministry of Energy, Thailand. Support from the Frontier Research Centre at VISTEC and the Synchrotron Light Research Institute (Public Organization) BL5.2 SUT-Nanotec-SLRI XAS beamline in Thailand for XANES are also acknowledged.

Conflict of Interest

The authors declare no conflict of interest.

Keywords: zinc-air batteries · bifunctional catalyst · trimetallic electrocatalyst · oxygen evolution reaction · oxygen reduction reaction

- [1] a) C. Hui, L. Mei-Ling, S. Chang-Yuan, L. Nan, L. Zhao-Qing, *Adv. Funct. Mater.* **2017**, *27*, 1701833; b) Y. Zhou, S. Xi, J. Wang, S. Sun, C. Wei, Z. Feng, Y. Du, Z. J. Xu, *ACS Catal.* **2018**, *8*, 673–677.
- [2] a) Y. Xue, S. Sun, Q. Wang, Z. Dong, Z. Liu, *J. Mater. Chem. A* **2018**, *6*, 10595–10626; b) P. G. Bruce, S. A. Freunberger, L. J. Hardwick, J.-M. Tarascon, *Nat. Mater.* **2011**, *11*, 19; c) X. Ji, L. F. Nazar, *J. Mater. Chem. A* **2010**, *20*, 9821–9826.
- [3] Y.-J. Li, L. Cui, P.-F. Da, K.-W. Qiu, W.-J. Qin, W.-B. Hu, X.-W. Du, K. Davey, T. Ling, S.-Z. Qiao, *Adv. Mater.* **2018**, *30*, 1804653.
- [4] a) X. Cai, L. Lai, J. Lin, Z. Shen, *Mater. Horiz.* **2017**, *4*, 945–976; b) Y. Yang, K. Mao, S. Gao, H. Huang, G. Xia, Z. Lin, P. Jiang, C. Wang, H. Wang, Q. Chen, *J. Adv. Mater.* **2018**, *30*, 1801732.
- [5] a) L. Yang, L. Shi, D. Wang, Y. Lv, D. Cao, *Nano Energy* **2018**, *50*, 691–698; b) K. Fujimoto, T. Okada, M. Nakayama, *J. Phys. Chem. C* **2018**, *122*, 8406–8413; c) T. Wang, Z. Kou, S. Mu, J. Liu, D. He, I. S. Amiinu, W. Meng, K. Zhou, Z. Luo, S. Chaemchuen, F. Verpoort, *Adv. Funct. Mater.* **2018**, *28*, 1705048.
- [6] D. U. Lee, P. Xu, Z. P. Cano, A. G. Kashkooli, M. G. Park, Z. Chen, *J. Mater. Chem. A* **2016**, *4*, 7107–7134.
- [7] a) X. Zhai, W. Yang, M. Li, G. Lv, J. Liu, X. Zhang, *Carbon* **2013**, *65*, 277–286; b) J. Zhang, C. Guo, L. Zhang, C. M. Li, *Chem. Commun.* **2013**, *49*, 6334–6336.
- [8] a) S. Kosasang, N. Ma, P. Wuamprakhon, N. Phattharasupakun, T. Maihom, J. Limtrakul, M. Sawangphruk, *Chem. Commun.* **2018**, *54*, 8575–8578; b) Y. Meng, W. Song, H. Huang, Z. Ren, S.-Y. Chen, S. L. Suib, *J. Am. Chem. Soc.* **2014**, *136*, 11452–11464.
- [9] I. Roche, E. Chaïnet, M. Chatenet, J. Vondrák, *J. Phys. Chem. C* **2007**, *111*, 1434–1443.
- [10] T. N. Lambert, J. A. Vigil, S. E. White, C. J. Delker, D. J. Davis, M. Kelly, M. T. Brumbach, M. A. Rodriguez, B. S. Swartzentruber, *J. Phys. Chem. C* **2017**, *121*, 2789–2797.
- [11] H. Gatemala, S. Kosasang, M. Sawangphruk, *Sustain. Ener* **2018**, *2*, 1170–1177.
- [12] a) L. Hu, H. Zhong, X. Zheng, Y. Huang, P. Zhang, Q. Chen, *Sci. Rep.* **2012**, *2*, 986; b) R. Miao, J. He, S. Sahoo, Z. Luo, W. Zhong, S.-Y. Chen, C. Guild, T. Jafari, B. Dutta, S. A. Cetegen, M. Wang, S. P. Alpay, S. L. Suib, *ACS Catal.* **2017**, *7*, 819–832.
- [13] a) Y. H. Ahmad, K. A. Eid, S. Y. AlQaradawi, N. K. Allam, *Sustain. Energy Fuels* **2017**, *1*, 1123–1129; b) Y. Deng, Z. Li, Z. Shi, H. Xu, F. Peng, G. Chen, *RSC Adv.* **2012**, *2*, 4645–4647.
- [14] a) M. Tadic, S. M. Savic, Z. Jaglicic, K. Vojisavljevic, A. Radojkovic, S. Prsic, D. Nikolic, *J. Alloys Compd.* **2014**, *588*, 465–469; b) P. N. Lisboa-Filho, M. Bahout, P. Barahona, C. Moure, O. Peña, *J. Phys. Chem. Solids* **2005**, *66*, 1206–1212.
- [15] a) G. Li, L. Xu, Y. Zhai, Y. Hou, *J. Mater. Chem. A* **2015**, *3*, 14298–14306; b) J.-G. Wang, Y. Yang, Z.-H. Huang, F. Kang, *J. Mater. Chem.* **2012**, *22*, 16943–16949; c) M. Huang, Y. Zhang, F. Li, Z. Wang, Alamusi, N. Hu, Z. Wen, Q. Liu, *Sci. Rep.* **2014**, *4*, 4518.
- [16] H. Zhu, D. Yu, S. Zhang, J. Chen, W. Wu, M. Wan, L. Wang, M. Zhang, M. Du, *Small* **2017**, *13*, 1700468.
- [17] Y.-L. T. Ngo, L. Sui, W. Ahn, J. S. Chung, S. H. Hur, *Nanoscale* **2017**, *9*, 19318–19327.
- [18] a) C. Dawei, Q. Man, L. Ying-Rui, H. Li, L. Dongdong, D. Chung-Li, L. Yafei, W. Shuangyin, *Angew. Chem. Int. Ed. Engl.* **2018**, *57*, 8691–8696; b) W. Hao-Fan, T. Cheng, W. Bin, L. Bo-Quan, Z. Qiang, *J. Adv. Mater.* **2017**, *29*, 1702327; c) J. Zhang, M. Zhang, L. Qiu, Y. Zeng, J. Chen, C. Zhu, Y. Yu, Z. Zhu, *J. Mater. Chem. A* **2019**, *7*, 19045–19059.
- [19] X.-Y. Yu, Y. Feng, B. Guan, X. W. Lou, U. Paik, *Energy Environ. Sci.* **2016**, *9*, 1246–1250.
- [20] a) T. Yang, J. Liu, R. Zhou, Z. Chen, H. Xu, S. Z. Qiao, M. J. Monteiro, *J. Mater. Chem. A* **2014**, *2*, 18139–18146; b) G. A. Ferrero, K. Preuss, A. B. Fuertes, M. Sevilla, M. M. Titirici, *J. Mater. Chem. A* **2016**, *4*, 2581–2589; c) Y. Liang, Y. Li, H. Wang, J. Zhou, J. Wang, T. Regier, H. Dai, *Nat. Mater.* **2011**, *10*, 780.
- [21] a) Y.-Q. Zhang, M. Li, B. Hua, Y. Wang, Y.-F. Sun, J.-L. Luo, *Appl. Catal. B* **2018**, *236*, 413–419; b) L. Xien, P. Minjoon, K. M. Gyu, G. Shiva, W. Gang, C. Jaephil, *Angew. Chem. Int. Ed. Engl.* **2015**, *54*, 9654–9658; c) Y. Bu, O. Gwon, G. Nam, H. Jang, S. Kim, Q. Zhong, J. Cho, G. Kim, *ACS Nano*

- [2017, 11, 11594–11601; d) J. Zhang, M. Zhang, Y. Zeng, J. Chen, L. Qiu, H. Zhou, C. Sun, Y. Yu, C. Zhu, Z. Zhu, *Small* 2019, 15, 1900307.
- [22] J. Xie, S. Li, X. Zhang, J. Zhang, R. Wang, H. Zhang, B. Pan, Y. Xie, *Chem. Sci.* 2014, 5, 4615–4620.
- [23] C. Hu, Q. Ma, S.-F. Hung, Z.-N. Chen, D. Ou, B. Ren, H. M. Chen, G. Fu, N. Zheng, *Chem* 2017, 3, 122–133.
- [24] a) Z. Luo, S. Lim, Z. Tian, J. Shang, L. Lai, B. MacDonald, C. Fu, Z. Shen, T. Yu, J. Lin, *J. Mater. Chem.* 2011, 21, 8038–8044; b) X. Min, Y. Chen, M. W. Kanan, *Phys. Chem. Chem. Phys.* 2014, 16, 13601–13604; c) S. Kosasang, N. Ma, N. Phattharasupakun, M. Sawangphruk, *J. Electrochem. Soc.* 2019, 166, A1543-A1549.
- [25] M. Sun, D. Davenport, H. Liu, J. Qu, M. Elimelech, J. Li, *J. Mater. Chem. A* 2018, 6, 2527–2539.
- [26] C. Su, W. Wang, Y. Chen, G. Yang, X. Xu, M. O. Tadé, Z. Shao, *ACS Appl. Mater. Interfaces* 2015, 7, 17663–17670.
- [27] a) P. Zhang, D. Bin, J.-S. Wei, X.-Q. Niu, X.-B. Chen, Y.-Y. Xia, H.-M. Xiong, *ACS Appl. Mater.* 2019, 11, 14085–14094; b) R. N. Singh, M. Kumar, A. S. K. Sinha, *Int. J. Hydrogen Energy* 2012, 37, 15117–15124.
- [28] a) A. Ajaz, J. Masa, C. Rösler, W. Xia, P. Weide, A. J. R. Botz, R. A. Fischer, W. Schuhmann, M. Muhler, *Angew. Chem. Int. Ed.* 2016, 55, 4087–4091; b) H.-F. Wang, C. Tang, X. Zhu, Q. Zhang, *J. Mater. Chem. A* 2016, 4, 3379–3385; c) G. Du, X. Liu, Y. Zong, T. S. A. Hor, A. Yu, Z. Liu, *Nanoscale* 2013, 5, 4657–4661; d) Y. J. Sa, K. Kwon, J. Y. Cheon, F. Kleitz, S. H. Joo, *J. Mater. Chem. A* 2013, 1, 9992–10001; e) C. Jin, F. Lu, X. Cao, Z. Yang, R. Yang, *J. Mater. Chem. A* 2013, 1, 12170–12177; f) M. G. Park, D. U. Lee, M. H. Seo, Z. P. Cano, Z. Chen, *Small* 2016, 12, 2707–2714; g) X. Chen, L. Wei, Y. Wang, S. Zhai, Z. Chen, S. Tan, Z. Zhou, A. K. Ng, X. Liao, Y. Chen, *Energy Storage Mater.* 2018, 11, 134–143; h) Y. He, J. Zhang, G. He, X. Han, X. Zheng, C. Zhong, W. Hu, Y. Deng, *Nanoscale* 2017, 9, 8623–8630; i) Z.-Q. Liu, H. Cheng, N. Li, T. Y. Ma, Y.-Z. Su, *Adv. Mater.* 2016, 28, 3777–3784; j) T. An, X. Ge, T. S. A. Hor, F. W. T. Goh, D. Geng, G. Du, Y. Zhan, Z. Liu, Y. Zong, *RSC Adv.* 2015, 5, 75773–75780; k) W. Hu, Q. Wang, S. Wu, Y. Huang, *J. Mater. Chem. A* 2016, 4, 16920–16927.
- [29] a) R. Qiao, T. Chin, S. J. Harris, S. Yan, W. Yang, *Curr. Appl. Phys.* 2013, 13, 544–548; b) M. Risch, K. A. Stoerzinger, B. Han, T. Z. Regier, D. Peak, S. Y. Sayed, C. Wei, Z. Xu, Y. Shao-Horn, *J. Phys. Chem. C* 2017, 121, 17682–17692; c) Y. Gorlin, B. Lassalle-Kaiser, J. D. Benck, S. Gul, S. M. Webb, V. K. Yachandra, J. Yano, T. F. Jaramillo, *J. Am. Chem. Soc.* 2013, 135, 8525–8534; d) A. Bergmann, I. Zaharieva, H. Dau, P. Strasser, *Energy Environ. Sci.* 2013, 6, 2745–2755; e) J. Huang, J. Chen, C. Fu, P. Cai, Y. Li, L. Cao, W. Liu, P. Yu, S. Wei, Z. Wen, J. Li, *ChemSusChem*, n/a.
- [30] I. Zaharieva, M. M. Najafpour, M. Wiechen, M. Haumann, P. Kurz, H. Dau, *Energy Environ. Sci.* 2011, 4, 2400–2408.
- [31] J. Messinger, J. H. Robblee, U. Bergmann, C. Fernandez, P. Glatzel, H. Visser, R. M. Cinco, K. L. McFarlane, E. Bellacchio, S. A. Pizarro, S. P. Cramer, K. Sauer, M. P. Klein, V. K. Yachandra, *J. Am. Chem. Soc.* 2001, 123, 7804–7820.
- [32] X. Han, X. Ling, D. Yu, D. Xie, L. Li, S. Peng, C. Zhong, N. Zhao, Y. Deng, W. Hu, *Adv. Mater.* 2019, 31, 1905622.
- [33] a) C. Wei, Z. Feng, G. G. Scherer, J. Barber, Y. Shao-Horn, Z. J. Xu, *Adv. Mater.* 2017, 29, 1606800; b) Z. Feng, W. T. Hong, D. D. Fong, Y.-L. Lee, Y. Yacoby, D. Morgan, Y. Shao-Horn, *Acc. Chem. Res.* 2016, 49, 966–973; c) N. Ma, S. Kosasang, A. Krittayavathananon, N. Phattharasupakun, S. Sethuraman, M. Sawangphruk, *Chem. Commun.* 2018; d) N. Ma, N. Phattharasupakun, J. Wuttiprom, C. Tangarnjanavalukul, P. Wuanprakhon, P. Kidkhunthod, M. Sawangphruk, *Electrochim. Acta* 2018, 271, 110–119; e) I. Zaharieva, D. González-Flores, B. Asfari, C. Pasquini, M. R. Mohammadi, K. Klingan, I. Zizak, S. Loos, P. Chernev, H. Dau, *Energy Environ. Sci.* 2016, 9, 2433–2443; f) P. Chomkuntod, N. Ma, S. Kosasang, S. Duangdangchote, N. Phattharasupakun, C. Jangsan, M. Sawangphruk, *ACS Appl. Energy Mater.* 2019.
- [34] a) D. C. Nguyen, D. T. Tran, T. L. L. Doan, D. H. Kim, N. H. Kim, J. H. Lee, *Adv. Energy Mater.*, n/a, 1903289; b) B. He, C. Xu, Y. Tang, Y. Qian, H. Liu, Q. Hao, Z. Su, *J. Mater. Chem. A* 2019, 7, 24964–24972; c) X. Qin, Z. Wang, J. Han, Y. Luo, F. Xie, G. Cui, X. Guo, X. Sun, *Chem. Commun.* 2018, 54, 7693–7696; d) X. Liu, M. Park, M. G. Kim, S. Gupta, G. Wu, J. Cho, *Angew. Chem. Int. Ed.* 2015, 54, 9654–9658; e) M. Prabu, K. Ketpang, S. Shanmugam, *Nanoscale* 2014, 6, 3173–3181; f) B. Chen, X. He, F. Yin, H. Wang, D.-J. Liu, R. Shi, J. Chen, H. Yin, *Adv. Funct. Mater.* 2017, 27, 1700795; g) J. Zhu, M. Xiao, Y. Zhang, Z. Jin, Z. Peng, C. Liu, S. Chen, J. Ge, W. Xing, *ACS Catal.* 2016, 6, 6335–6342; h) S. K. Singh, V. M. Dhavale, S. Kurungot, *ACS Appl. Mater. Interfaces* 2015, 7, 21138–21149.

Manuscript received: January 10, 2020

Revised manuscript received: February 26, 2020

Accepted manuscript online: February 27, 2020

Version of record online: March 10, 2020